

# High-Performance Liquid Metal/Polyborosiloxane Elastomer toward Thermally Conductive Applications

Chunyu Zhao, Yu Wang,\* Liang Gao, Yunqi Xu, Ziyang Fan, Xujing Liu, Yong Ni, Shouhu Xuan, Huaxia Deng,\* and Xinglong Gong\*



Cite This: *ACS Appl. Mater. Interfaces* 2022, 14, 21564–21576



Read Online

ACCESS |



Metrics & More



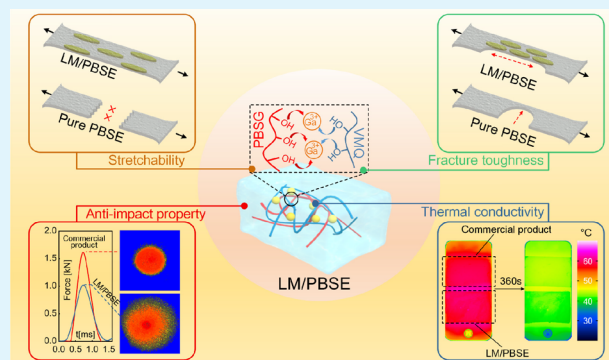
Article Recommendations



Supporting Information

**ABSTRACT:** With the combination of high flexibility and thermal property, thermally conductive elastomers have played an important role in daily life. However, traditional thermally conductive elastomers display limited stretchability and toughness, seriously restricting their further development in practical applications. Herein, a high-performance composite is fabricated by dispersing room-temperature liquid metal microdroplets (LM) into a polyborosiloxane elastomer (PBSE). Due to the unique solid–liquid coupling mechanism, the LM can deform with the PBSE matrix, achieving higher fracture strain (401%) and fracture toughness (2164 J/m<sup>2</sup>). Meanwhile, the existence of LM microdroplets improves the thermal conductivity of the composite. Interestingly, the LM/PBSE also exhibits remarkable anti-impact, adhesion capacities under complex loading environments. As a novel stretchable elastomer with enhanced mechanical and thermal behavior, the LM/PBSE shows good application prospects in the fields of thermal camouflages, stretchable heat-dissipation matrices, and multifunctional shells for electronic devices.

**KEYWORDS:** liquid metal, polyborosiloxane elastomer (PBSE), solid–liquid coupling composite, mechanical property optimization, thermally conductive application



## 1. INTRODUCTION

With the continuous development of wearable devices,<sup>1,2</sup> flexible electronics,<sup>3–5</sup> and smart thermal management,<sup>6,7</sup> the demand for high-performance stretchable elastomers as thermal conductive components has become increasingly prominent in practical applications. Generally, the thermally conductive material is fabricated by embedding rigid conductive agents, such as carbonyl iron (CI),<sup>8</sup> boron nitride (BN),<sup>9</sup> aluminum nitride (AlN),<sup>10</sup> and graphene/cellulose nanofiber (CNFG)<sup>11</sup> into the polymer matrixes. However, the stiffness mismatch between the rigid fillers and matrixes often reduces the overall stretchability of the thermally conductive elastomers. Besides, the excessive addition of conductive agents also seriously affects the flexibility and density of the composite.<sup>12</sup> Therefore, the thermal-mechanical trade-off is still a challenge for thermally conductive materials.

Liquid metal (LM), composed of low-melting eutectic gallium–indium (EGaIn), is a liquid-phase alloy with non-toxicity, high electrical conductivity, environmental stability, and biocompatibility.<sup>13–17</sup> Recent research demonstrates that the LM droplets can be stably encapsulated in the specific elastomers due to the combinations of Ga<sup>3+</sup> with certain oxygen-containing groups from the polymer matrix.<sup>18</sup> In contrast to the rigid-particle reinforced elastomer, the LM

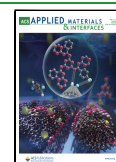
can adjust its morphology with the deformation of the matrix, and the elastomers achieve a higher stretchability due to this unique solid–liquid coupling mechanism.<sup>19</sup> Kazem et al. also prove that the embedding of LM can effectively improve the fracture toughness for the Ecoflex elastomer.<sup>20</sup> Meanwhile, resulting from the high thermal conductivity of the LM, the introduction of LM overcomes the constraint of poor heat transfer for soft dielectric materials.<sup>21</sup>

In terms of practical application, the LM reinforced composite is expected to be used as the thermally conductive interface material. The LM reinforced composite is not only required to possess remarkable mechanical behavior under the quasi-static loading conditions but also to have good adaptability to complex loading environments.<sup>18</sup> So far, the Ecoflex and Polydimethylsiloxane (PDMS) elastomers are the common matrix materials for LM inclusions. However, traditional LM reinforced composites are easy to separate

Received: March 21, 2022

Accepted: April 15, 2022

Published: April 27, 2022



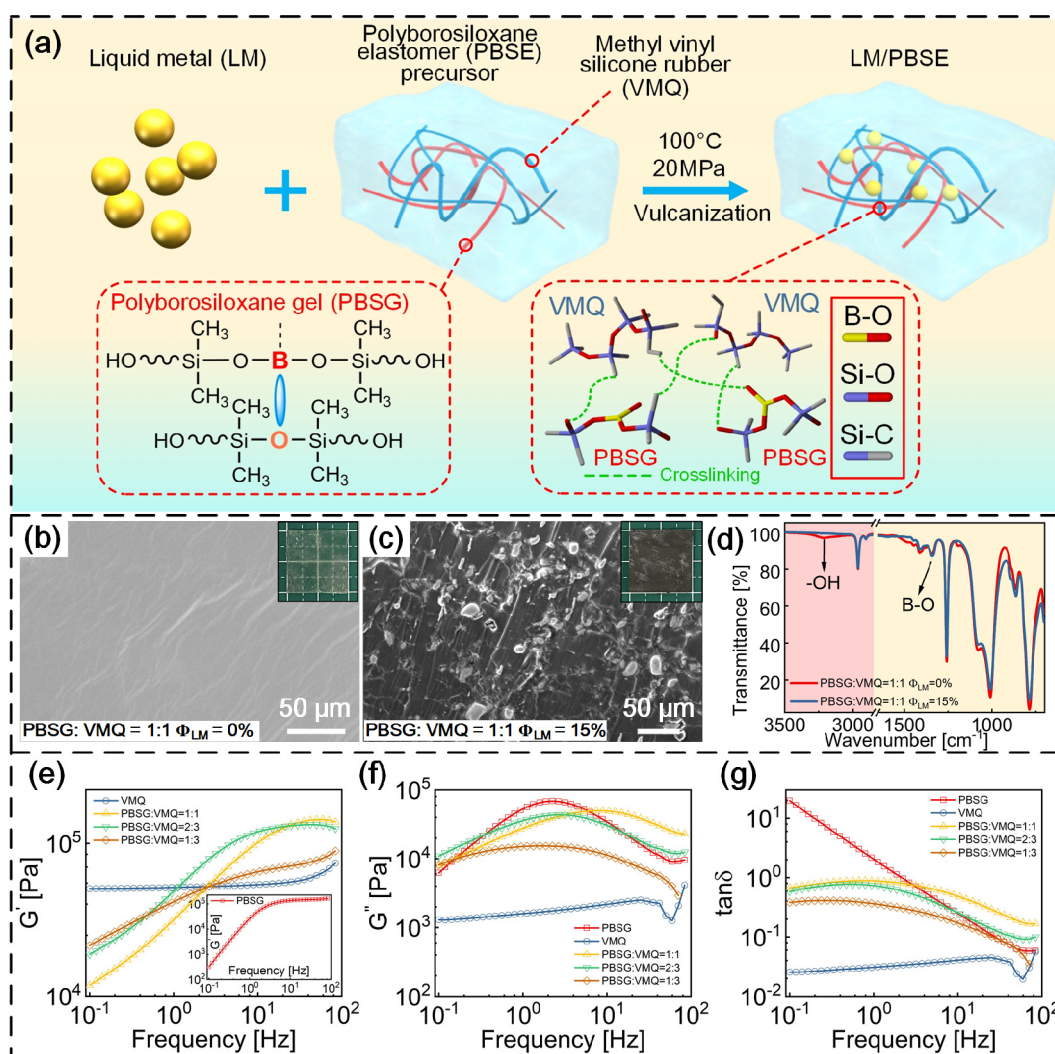


**Figure 1.** Fabrication and Rheological Behavior of LM/PBSE. (a) Illustration of the fabrication method for LM/PBSE. (b,c) SEM image of pure PBSE (PBSG:VMQ = 1:1,  $\Phi_{LM} = 0\%$ ) and LM/PBSE (PBSG:VMQ = 1:1,  $\Phi_{LM} = 15\%$ ); The insets are the digital images of PBSE and LM/PBSE with the dimension of 20 mm  $\times$  20 mm  $\times$  1 mm). (d) The FTIR of the pure PBSE and LM/PBSE. (e–g) Rheological results of storage modulus ( $G'$ ), loss modulus ( $G''$ ), and  $\tan \delta$  value for PBSG, VMQ, and PBSE matrixes under sweeping frequency test.

from their body materials under the conditions of heating and vibration due to their weak adhering ability. Besides, the mechanical properties for most of the LM reinforced composites are strain-rate independent, which results in their limited anti-impact property against impulsive loadings.<sup>22,23</sup> Therefore, exploring high-performance matrixes with unique mechanical properties, such as adhesive and anti-impact capability, becomes a top priority.

Recently, the polyborosiloxane elastomer (PBSE), a supra-molecular material, has attracted considerable industrial and academic interest due to its thermodynamically stable backbone.<sup>24</sup> Because of the dynamic evolutions of the boron–oxygen (B–O) dative bond, rapid and reversible response to the variation of external strain rates through the change of modulus can be made by the PBSE.<sup>25</sup> Besides, the PBSE has also been proved to have long-term adhesion stability and self-adhering ability.<sup>26</sup> Therefore, it is of great scientific value to fabricate a novel LM-based thermally conductive elastomer using the PBSE matrix.

Herein, the LM droplets are successfully dispersed into the PBSE for the first time through a blending-vulcanizing method. First, the influences of LM content and matrix component on

the material behavior of PBSE composite are detailedly studied through uniaxial tensile testing, crack propagation testing, as well as thermal conductivity testing. Second, the anti-impact and adhesion properties of LM/PBSE with the optimal proportion of LM and PBSE are also characterized to show its remarkable adaptability to complex loading environments. Finally, potential applications of LM/PBSE in thermal camouflages, stretchable thermal dissipation matrixes, and high-performance shells for electronic devices are further proposed.

## 2. EXPERIMENTAL SECTION

**2.1 Materials.** Liquid metal (LM, eutectic of gallium, indium, and tin with a melting point of 11 °C) was purchased from Dongguan Dinguan Metal Technology Co., Ltd. China. Hydroxyl silicone oil with a molecular weight of 4000 Da was purchased from Jining Huakai Resin Co., Ltd. China. Methyl vinyl silicone rubber (VMQ 110–2) was purchased from Shenzhen Muwei Technology Co., Ltd. China. Boric acid and benzoyl peroxide (BPO) were purchased from Sinopharm Chemical Reagent Co. Ltd. China.

**2.2. Synthetic Method for LM/PBSE.** First, the boric acid and hydroxyl silicone oil were manually stirred into a homogeneous mixture in an enamel ware with a mass ratio of 1:20. Then, the

mixture was heated at 180 °C for 2 h in an oven (KSL-1100X-S, Hefei Kejing Material Technology Co., Ltd. China). During the heating process, polymerization occurred between boric acid and hydroxyl silicone oil. After cooling down the mixture to room temperature for another 30 min, the plasticine-like polyborosiloxane gel (PBSG) was obtained. After that, different contents of PBSG and VMQ (mass ratio of PBSG: VMQ = 1:1, 2:3, 1:3) were stirred mechanically in an internal mixer machine (HL-200, Jilin University. China) at 40 rpm with 2.0% w.t. of BPO as the vulcanizing agent to prepare the precursor of PBSE elastomer. Meanwhile, different contents of LM (volume fraction of  $\Phi_{LM} = 0, 1, 5, 10, \text{ and } 15\%$ ) were dispersed dropwise into the PBSG-VMQ using a dropper. The mixture was stirred for about 30 min until no LM agglomeration occurred. Next, the mixture was vulcanized in a plate vulcanizing machine (YS20T-S, Xushuai Precision Technology Co., Ltd. China) using customized stainless steel molds under the reaction conditions of 100 °C and 20 MPa for 15 min to form cross-links between polymer chains. During the process, the vulcanizing agent BPO promoted the cross-links between methyl–methyl, methyl–vinyl, and vinyl–vinyl in the VMQ precursor. Besides, according to the previous research, the hydroxide radical from the VMQ could further combine with PBSG to form Si–O–Si, Si–O–B skeletons.<sup>27</sup> Finally, the LM/PBSE elastomer was obtained after the cooling and demolding operations (Figure 1a). The VMQ precursor with 2.0% w.t. of BPO was also vulcanized under the same condition to obtain VMQ elastomer.

**2.3. Characterization.** The rheological measurements were performed on a rotational rheometer (Physica MCR 302, Anton Paar Co. Austria) using a 20 mm PP20 parallel plate at a temperature of 25 °C. Oscillation shear mode at an amplitude of 1% was chosen, and the frequency range was from 0.1 to 100 Hz with a logarithmic growth.

The uniaxial tensile and cyclic measurements were performed on a universal electronic material testing machine (Criterion Model 43, MTS Co., Ltd. China) with a 500 N force sensor module. The clamped region for the specimen was 40 mm × 20 mm × 2 mm in dimension, and the loading strain rate was set as 0.01 s<sup>-1</sup> according to ISO 37:2017. In the uniaxial tensile test, the specimen was stretched until broken. Moreover, in the cyclic loading and unloading test, the stretching amplitude was  $\epsilon = 0.1, 0.2, 0.3, 0.4, \text{ and } 0.5$ , respectively. The loading strain rate was also set to be 0.01 s<sup>-1</sup>.

The crack propagation analyses were also performed on the aforementioned universal material testing machine. The specimen in the crack propagation test was 70 mm × 20 mm × 1 mm in dimension, and a 15 mm initial crack was preset at one end of the specimen. Besides, the black speckles were randomly sprayed on the specimen surface in the undeformed status. During the crack propagation, the deformation history of the black speckles was recorded by a high-resolution CCD camera (MV-CA050-11UM, Hikvision. China) with a spatial resolution of 27.84  $\mu\text{m}$ . Then, the strain field of the notched specimen was calculated by Ncorr software.

The thermal conductivity measurements were conducted on a laser thermal conductometer (LFA457, Netzsch, Germany). During the test, the dimension of the specimen was 20 mm × 20 mm × 4 mm, and the thermal conductivity was calculated through the classical laser flash analytical method. At a given temperature, the laser source emitted a light pulse and irradiated it evenly on the lower surface of the specimen. The temperature of the lower surface increased instantly after absorbing light energy and propagated the energy to the cold end (upper surface) by one-dimensional heat conduction. The corresponding temperature-rise process at the upper surface was continuously measured by an infrared detector. Through the thermal test module in the laser thermal conductometer, the thermal diffusion coefficient  $\alpha(T)$ , specific heat  $C_p(T)$ , and density  $\rho(T)$  of the specimen were measured, respectively. Based on the formula of  $k = \alpha(T) \cdot C_p(T) \cdot \rho(T)$ , the thermal conductivity of the material could be calculated.

The drop impact measurements were operated on an automatic drop tower testing machine (ZCJ-1302-A, MTS Co., Ltd. China) with a 30 kN force sensor. A 0.33 kg standard drop tower was used to investigate the anti-impact behavior of the specimen. The specimen

with the dimension of 20 mm × 20 mm × 4 mm was attached to the upper surface of the sensor. During the impact process, the drop tower was released from specific heights (10, 20, and 30 cm) and impacted the center of the specimen.

The micromorphology and related energy-dispersive X-ray spectrum (EDS) were observed on scanning electron microscopy (SEM 500, Carl Zeiss Microscopy Ltd. UK). The stretchability of LM under uniaxial tension and the self-adhering process were recorded by a digital microscope (Keyence VHX, VH-Z100, Japan). The micromorphology of LM at the crack-tip region was observed by a transmission microscope (Nikon-TIS, Japan). The Fourier transform infrared spectroscopy (FTIR) was recorded by an infrared spectrum instrument (TL-9000, PerkinElmer, U.S.) with the wavenumbers ranging from 750 to 3500 cm<sup>-1</sup>. The temperature field was calculated by an infrared thermal imager (ImageIR 832S, InfraTec, Germany).

### 3. RESULTS AND DISCUSSION

**3.1. Fabrication and Rheological Behavior of LM/PBSE.** The LM/PBSE is fabricated by dispersing liquid phase LM into the PBSE precursor through a blending-vulcanizing method. Due to the interactions between the LM and PBSE precursor, the LM/PBSE displays an elastomer state with stable geometric dimensions in the natural state. From the SEM image, the LM droplets are evenly distributed in the PBSE with an average diameter of 15.48  $\mu\text{m}$  (Figure 1b,c, Supporting Information (SI) Figure S1). The elementary composition of LM/PBSE is also analyzed by the energy dispersive spectrometer (EDS) mapping. The results indicate that the LM is mainly composed of Ga, In, and Sn metal elements, while the PBSE matrix is a classical siloxane system containing Si and O elements (SI Figure S2). During the vulcanization process, the Ga<sup>3+</sup> in liquid phase LM can coordinate with the oxygen-containing groups from the PBSE matrix proven by the weak absorption peak of –OH (3215 cm<sup>-1</sup>) in the FT-IR spectra (Figure 1d). The enhanced interfacial adhesions between the liquid LM and the solid matrix can effectively prevent the leak of LM from the PBSE polymer networks. Notably, adding excess LM can lead to droplet aggregation. A complete cross-linking reaction between the agglomerating LM and the matrix is difficult to achieve. Therefore, partial unformed regions can be observed after the vulcanization. Meanwhile, since the density of LM ( $\rho_{LM} = 6100 \text{ kg/m}^3$ ) is much higher than that of the PBSE matrix ( $\rho_{PBSE} = 1000 \text{ kg/m}^3$ ), the higher content of LM in the PBSE matrix also violates the lightweight concept for the polymer elastomer. Based on the above two reasons, the maximum volume fraction of LM dispersed in the PBSE matrix is set to be 15% in this work. The corresponding relationship between the LM volume fraction and the mass fraction is described in SI Table S1.

First, the sweeping frequency experiments are carried out to analyze the effects of matrix components and LM contents on the rheological behavior of the LM/PBSE composite. Interestingly, the existence of boron–oxygen (B–O) dynamic bonds from PBSG endows the PBSE matrix with a unique strain-rate stiffening behavior.<sup>26,28</sup> For the single-phase PBSG component, the storage modulus ( $G'$ ) rapidly increases from  $3.1 \times 10^2 \text{ Pa}$  to  $6.1 \times 10^5 \text{ Pa}$  and then reaches the platform period, displaying a typical strain-rate stiffening property (Figure 1e). The initial loss modulus ( $G''$ ) is much larger than  $G'$ , while the value of  $G''$  increases initially, followed by an decrease with the increase of frequency (Figure 1f). However, the vulcanized VMQ component exhibits a strain-rate independent effect with approximately stable  $G'$  ( $5.0 \times 10^4$

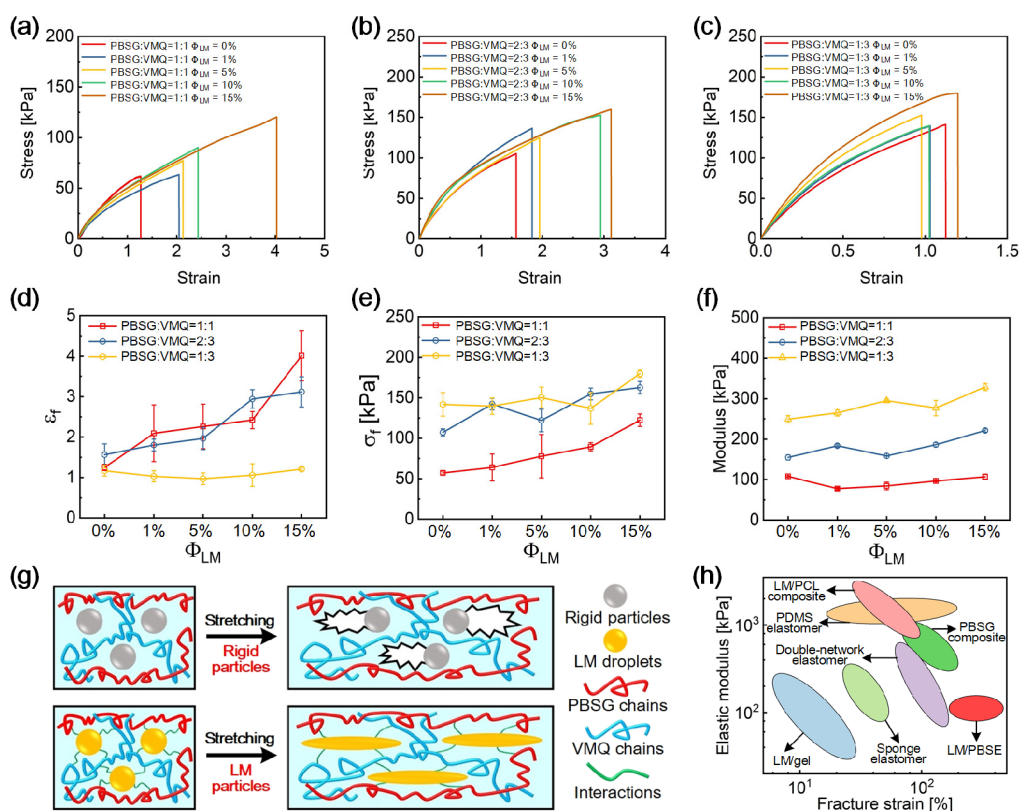


**Figure 2.** Quasi-Static Uniaxial Loading Property of LM/PBSE. (a–c) Stress–strain curves of different LM/PBSE elastomers. (d–f) Calculated fracture strain  $\epsilon_f$ , fracture stress  $\sigma_f$ , and modulus of different LM/PBSE elastomers (the modulus is defined as the secant modulus at the strain of  $\epsilon = 0.25$ , Error bars: SD,  $n = 3$ ). (g) Illustration between the LM/PBSE elastomer and rigid-particle reinforced composites during the tensile process. (h) Comparison of tensile properties among the LM/PBSE with relevant elastomers.

Pa) and  $G''$  ( $2.0 \times 10^3$  Pa). The ratio of  $G'$  to  $G''$  is defined as the loss factor ( $\tan \delta = G''/G'$ ). When  $\tan \delta > 1$ , the material is considered to be in a viscous state, while the material transforms into an elastic state once  $\tan \delta \leq 1$ . The smaller the  $\tan \delta$  value, the closer the material is to the ideal elastic state.<sup>29</sup> It is demonstrated that the PBSG exhibits a viscous state at low frequency, but the material changes into an elastic state with the increase of frequency. In contrast, the VMQ retains an elastic state within the test frequency range.

The rheological behavior of the PBSE matrix is between those of single network components.<sup>27</sup> The PBSE overcomes the cold flow effect of PBSG at low frequency and still maintains a strain-rate stiffening effect at high frequency (Figure 1g, SI Figure S3). Since the initial storage modulus ( $G'_0$ ) for PBSG is much lower than VMQ, while the maximum storage modulus ( $G'_{max}$ ) of PBSG in the high-frequency region is larger than VMQ. The PBSE with higher content of PBSG displays a lower  $G'_0$  and a more obvious relative strain-rate stiffening effect ( $G'_{max} - G'_0$ ). Besides, the addition of various contents of LM had little effect on the rheological behavior of the PBSE matrixes (SI Figure S4). In contrast to the traditional particle-reinforced elastomer, whose  $G'_0$  significantly improved with the increase of particle contents,<sup>30</sup> the LM/PBSE maintains good flexibility in the natural state even at high  $\Phi_{LM}$  values due to the low modulus and liquid property of LM. Meanwhile, the composite also showed a typical strain-rate stiffening behavior under high-frequency loadings.

**3.2. Quasi-Static Uniaxial Loading Property of LM/PBSE.** The stress–strain curves of three PBSE matrixes with different LM contents are obtained through the quasi-static

uniaxial tensile test (Figure 2a–c). For the PBSE matrix (PBSG: VMQ = 1:1), the volume fraction of LM ( $\Phi_{LM}$ ) has a significant effect on the tensile behavior of the composite. The fracture strain ( $\epsilon_f$ ) and fracture stress ( $\sigma_f$ ) of LM/PBSE increases with the growth of  $\Phi_{LM}$ . In contrast to the pure PBSE matrix ( $\Phi_{LM} = 0\%$  PBSE) with limited  $\epsilon_f = 1.24$  and  $\sigma_f = 57.23$  kPa, the  $\epsilon_f$  and  $\sigma_f$  of LM/PBSE are improved to  $\epsilon_f = 4.01$  and  $\sigma_f = 122.34$  kPa when  $\Phi_{LM}$  is 15%. With a higher content of VMQ (PBSG: VMQ = 2:3), the improvement of tensile behavior becomes less obvious with the increase of  $\Phi_{LM}$  (from  $\epsilon_f = 1.56$  at  $\Phi_{LM} = 0\%$  to  $\epsilon_f = 3.12$  at  $\Phi_{LM} = 15\%$ ). Particularly, for the PBSE matrix (PBSG: VMQ = 1:3), the increment of  $\Phi_{LM}$  even has little effect on the stretchability of the LM/PBSE composite (Figure 2d,e). Therefore, the introduction of LM can optimize the stretchability of the PBSE matrix (PBSG: VMQ = 1:1) to the greatest extent (SI Figure S5). Similar to the rheological results, the flexibility of the PBSE matrix is positively correlated with the PBSG content, and the  $\Phi_{LM}$  shows little influence on the tensile modulus of the PBSE matrix under quasi-static loadings (Figure 2f). By utilizing microscopic observation technology, the LM droplets are proved to deform with the PBSE matrix (PBSG: VMQ = 1:1) during the tensile process (Figure 2g, SI Figure S6). Based on this unique solid–liquid coupling mechanism, the LM/PBSE overcomes the inhomogeneous deformation caused by particles peeling from the matrix in traditional particle-reinforced elastomers. The composite can keep structural integrity under large deformation and achieve a higher stretchability. With the increment of  $\Phi_{LM}$ , more regions in the LM/PBSE participates in the solid–liquid coupling effect

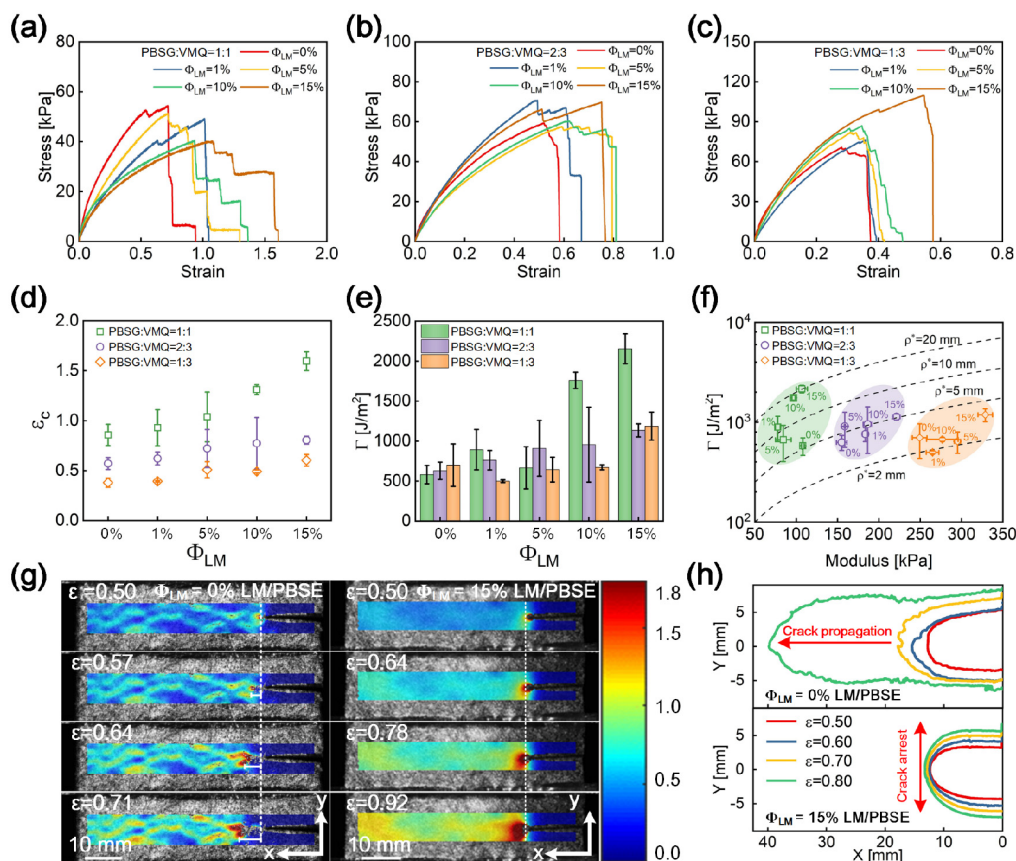


**Figure 3.** Crack Propagation Behavior of LM/PBSE. (a–c) Stress–strain curves for notched LM/PBSE elastomers with different matrixes and  $\Phi_{LM}$ . (d–e) Calculated critical strain  $\epsilon_c$ , fracture toughness  $\Gamma$  (error bars: S.D.,  $n = 3$ ). (f) Relation between the fracture toughness and modulus of different notched LM/PBSE elastomers with precuts (dashed lines correspond to the elasto-adhesive scale,  $\rho^*$ ). (g–h) The strain field contours and crack tip morphologies for pure PBSE matrix ( $\Phi_{LM} = 0\%$ , LM/PBSE) and LM/PBSE ( $\Phi_{LM} = 15\%$ , LM/PBSE).

during the tensile process, resulting in a positive correlation between the  $\epsilon_f$  and  $\Phi_{LM}$ . The mechanical performance of LM/PBSE is also compared with some common elastomer composites, such as PDMS elastomer,<sup>31,32</sup> double-network elastomer,<sup>33</sup> PBSE base composite,<sup>34</sup> sponge elastomer,<sup>35</sup> LM/gel,<sup>36</sup> and LM/PCL.<sup>37</sup> It is demonstrated that the LM/PBSE fabricated in this work achieves a higher fracture strain while maintaining good flexibility (Figure 2h).

The strain–stress hysteresis curve of the LM/PBSE with different LM components is also evaluated through a series of uniaxial cycling loadings from  $\epsilon = 0.1$  to 0.5 (SI Figure S7). The energy dissipated density and energy dissipation rate are calculated from the hysteresis loops. Due to the viscous effect of PBSE at low strain rates, the PBSE matrix with higher content of PBSE (PBSG: VMQ = 1:1) shows a higher energy dissipation rate than the other two PBSE matrixes. Additionally, the energy dissipation rate of the composite can be further improved with the dissipation of LM, especially when  $\Phi_{LM} = 15\%$  (SI Figure S8). Therefore, the LM/PBSE composite (PBSG: VMQ = 1:1,  $\Phi_{LM} = 15\%$ ) also possesses a high damping property under quasi-static uniaxial loadings.

**3.3. Crack Propagation Behavior of LM/PBSE.** The fracture toughness of LM/PBSE with different matrix components and  $\Phi_{LM}$  is also investigated by the crack propagation test.<sup>38,39</sup> During the test, the specimen with an initial crack is stretched at a constant strain rate of  $0.01 \text{ s}^{-1}$ , and cracks for all specimens propagated perpendicular to the loading direction, showing typical penetrating crack morphol-

ogies (SI Figure S9). Notably, the critical strain ( $\epsilon_c$ ) is defined as the strain until the LM/PBSE was destroyed. It is illustrated from the stress–strain curves that the softer LM/PBSE (PBSG: VMQ = 1:1) displays a better anti-crack ability compared to the other two stiffer matrixes (PBSG: VMQ = 2:3 and PBSG: VMQ = 1:3) (Figure 3a–c). The  $\epsilon_c$  is larger for the softer LM/PBSE at the same  $\Phi_{LM}$  value, and a more apparent stepwise reduction is observed in the stress attenuation process. Moreover, the  $\epsilon_c$  values are sensitive to  $\Phi_{LM}$  for the softer LM/PBSE. The critical strain increases from  $\epsilon_c = 0.86$  to  $\epsilon_c = 1.60$  with the increment of  $\Phi_{LM}$ , while the enhancement effect of  $\epsilon_c$  is relatively limited for the stiffer matrixes (PBSG: VMQ = 2:3 and PBSG: VMQ = 1:3) (Figure 3d). Another unnotched specimen with the same dimension is stretched to the same  $\epsilon_c$  to calculate the fracture toughness of the LM/PBSE. The  $\Gamma$  is obtained by multiplying the integral of the stress–strain curve for unnotched LM/PBSE by the height of the specimen (eq 1) (SI Figure S10).<sup>40</sup>

$$\Gamma = h_0 W(\epsilon) = h_0 \int_{\epsilon=0}^{\epsilon=\epsilon_c} \sigma(\epsilon) d\epsilon \quad (1)$$

For the pure PBSE matrix, the entanglements and interpenetrating interactions among the polymer chains are the main mechanisms to resist crack tip propagation. Still, this form of energy dissipation is quite limited. Interestingly, with the addition of LM into the softer PBSE matrix (PBSG: VMQ = 1:1), the toughness values of the specimens significantly enhance when  $\Phi_{LM} \geq 10\%$ . The fracture toughness reaches  $\Gamma$

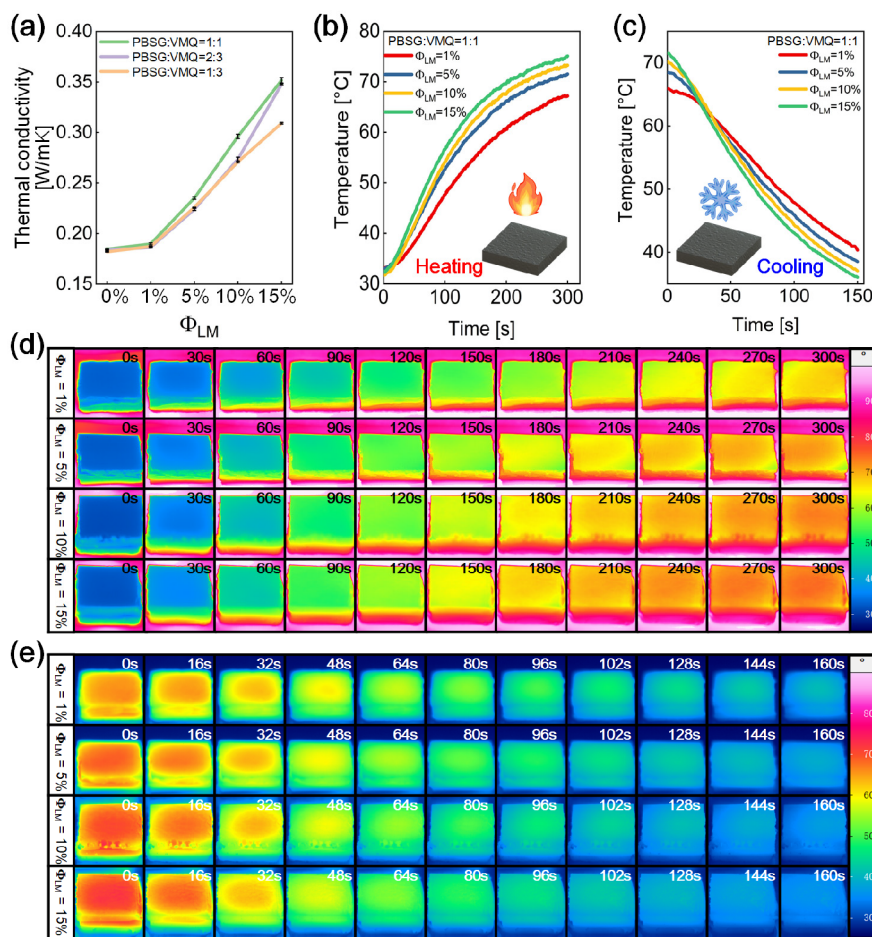


**Figure 4.** Thermal Property of LM/PBSE Elastomer. (a) Calculation of thermal conductivity based on the laser flash analytical method for different PBSE matrixes with different  $\Phi_{LM}$  (Error bars: S.D.,  $n = 3$ ). (b,c) The temperature in the center region of specimens (PBSG: VMQ = 1:1) with different  $\Phi_{LM}$  during the heating and cooling process. (d,e) Corresponding evolutions of full-field temperature distributions on the surface of specimens during the heating and cooling process.

= 1875 J/m<sup>2</sup> at  $\Phi_{LM} = 10\%$  and  $\Gamma = 2164$  J/m<sup>2</sup> at  $\Phi_{LM} = 15\%$ , much higher than the pure matrix of  $\Gamma = 673$  J/m<sup>2</sup>. Besides, for the other two stiffer PBSE matrixes (PBSG: VMQ = 2:3 and PBSG: VMQ = 1:3), the introduction of LM can also improve the fracture toughness of the composite. Since the  $\varepsilon_c$  of the LM/PBSE is only slightly improved under these two ratios, the enhancement effect of  $\Gamma$  is relatively limited (Figure 3e). To further investigate the toughening mechanism of LM, another LM/PBSE elastomer (PBSG: VMQ = 1:1,  $\Phi_{LM} = 15\%$ ) is fabricated using the solid LM inclusions (eutectic of bismuth, indium, and tin with a melting point of 60 °C, purchased from Dongguan Dingguan Metal Technology Co., Ltd. China). Under the circumstance, the solid inclusions are regarded as the particle reinforced phase. Due to the solid inclusions and matrix interaction, the composite also achieves a higher toughness. However, this toughening mechanism is still limited compared to the LM/PBSE elastomer using liquid inclusions (SI Figure S11). The liquid phase LM can be elongated along the loading direction resulting from the stretchability of liquid inclusions. Due to strong interfacial bondings between the LM and PBSE matrix, the crack tip is forced to deflect along with the interface until the LM slides out of the matrix (SI Figure S12). A wider region near the crack tip is involved in the resistance against the crack propagation, leading to a higher fracture toughness value.

The toughening mechanism also can be quantitatively proved by the elasto-adhesive scale  $\rho^*$ , defined as the ratio of fracture energy to the tensile modulus (calculated in Section 3.2) (eq 2).<sup>41</sup>

$$\rho^* = \frac{\Gamma}{E_T} \quad (2)$$

The  $\rho^*$  describes the characteristic length near the crack tip that experiences large deformation. The higher the value of  $\rho^*$ , the greater the tear resistance to crack propagation. For the PBSE matrix (PBSG: VMQ = 1:1) embedded with the same volume fraction of LM ( $\Phi_{LM} = 15\%$ ), the  $\rho^*$  of solid inclusions is 5.38 mm, while the  $\rho^*$  of liquid inclusions increases to 20.18 mm. The liquid phase LM reinforced PBSE exhibits a higher anti-crack ability. Besides, the matrix of PBSG: VMQ = 1:1 also shows a higher  $\rho^*$  value than the other two stiffer matrixes, verifying the superiority of the softer matrix in crack resistance (Figure 3f).

Utilizing the digital image correlation (DIC) method, the toughening mechanism also can be explained based on the evolution of the crack tip.<sup>42</sup> The strain fields for LM/PBSE with different  $\Phi_{LM}$  values (PBSG: VMQ = 1:1,  $\Phi_{LM} = 0\%$  and PBSG: VMQ = 1:1,  $\Phi_{LM} = 15\%$ ) were compared. Notably, the red region in the strain contours corresponds to the strain field near the crack tip. With the increase of the tensile strain, only a

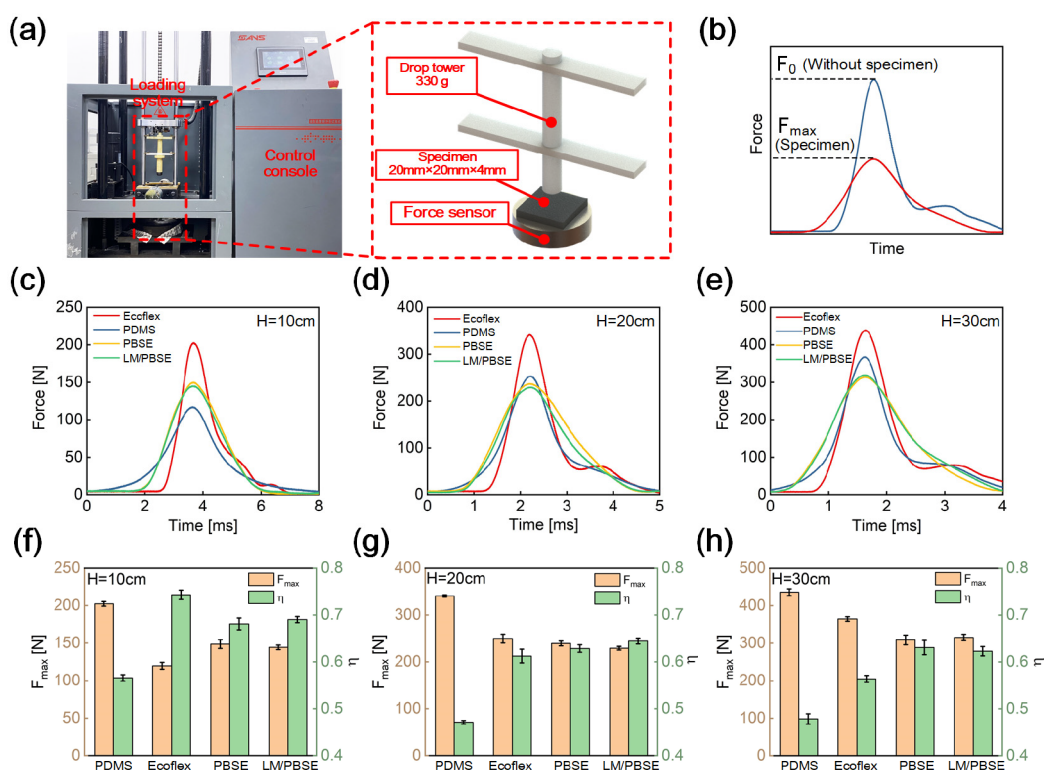


**Figure 5.** Anti-impact Property of LM/PBSE. (a) Experimental platform of drop-tower impact devices (b) Definitions of the peak backing force of control group ( $F_0$ ), experimental group ( $F_{max}$ ). (c–e) Force-time curves of PDMS, Ecoflex, pure PBSE matrix, and LM/PBSE at different releasing heights. (f–h) Statistics of  $F_{max}$  and  $\eta$  values of PDMS, Ecoflex, pure PBSE matrix, and LM/PBSE at different releasing heights (Error bars: SD,  $n = 3$ ).

small amount of high strain region accumulates near the crack tip for the pure PBSE matrix. Furthermore, the movement of the high strain region confirms the rapid propagation of the crack tip when  $\varepsilon > 0.50$ . However, the strain field evolution for the LM/PBSE is quite different. More and more high strain regions are generated near the crack tip following the growth of tensile strain. There is no obvious propagation at the crack tip until  $\varepsilon = 0.92$  (Figure 3g). The crack tip opening displacement (CTOD) is also calculated based on a frame-by-frame analysis of crack tip morphologies. It is demonstrated that the addition of LM can improve the crack initiation strain for the PBSE matrix (SI Figure S13). In the strain range of  $\varepsilon = 0.5$  to 0.8, a rapid crack propagation phenomenon is observed in the pure PBSE. On the contrary, the crack tip motion in the LM/PBSE composite is effectively constrained through the sideways extension along the loading direction, leading to a higher crack initiation strain (Figure 3h, SI Figure S14, and SI Movie S1).

**3.4. Thermal Properties of LM/PBSE Elastomer.** It is known that the LM possesses a high thermal conductivity, while the thermal conductivity for the silicone elastomer is generally low.<sup>43</sup> Based on the laser flash analytical (LFA) method,<sup>44</sup> the influence of  $\Phi_{LM}$  on the thermal conductivity of the PBSE matrix is investigated. According to the previous report,<sup>21</sup> there is a positive correlation between the thermal conductivity and  $\Phi_{LM}$  for all PBSE matrixes. At the same  $\Phi_{LM}$  level, the thermal conductivity for the softer PBSE (PBSG: VMQ = 1:1) is slightly higher than the other two matrixes. For the matrix of PBSG: VMQ = 1:1, the thermal conductivity of LM/PBSE at  $\Phi_{LM} = 15\%$  is 0.35 W/mK, approximately twice as large as the pure matrix (0.19 W/mK) (Figure 4a). Meanwhile, the heating and cooling process of specimens

(PBSG: VMQ = 1:1) with different  $\Phi_{LM}$  is also recorded by an infrared thermal imager to discuss the thermal effect of LM/PBSE (Figure 4b,c). Considering that the transparency of the PBSE matrix inevitably influences the setting of emissivity parameters, the nontransparent specimens with a black surface ( $\Phi_{LM} = 1, 5, 10,$  and  $15\%$ ) are selected for comparison. During the heating process, all specimens are placed on a heating plate of  $100\text{ }^\circ\text{C}$ . It is illustrated that the temperature of the LM/PBSE with higher  $\Phi_{LM}$  increases faster in the central area of the surface. It takes only 118 s for the LM/PBSE with  $\Phi_{LM} = 15\%$  to heat from  $32$  to  $60\text{ }^\circ\text{C}$ . However, the same heating process takes about twice as long for the LM/PBSE with  $\Phi_{LM} = 1\%$ . Regarding the cooling process, the heated specimens are cooled on a  $25\text{ }^\circ\text{C}$  plate. The LM/PBSE of  $\Phi_{LM} = 15\%$  with the highest initial temperature reaches the lowest end temperature at the ending point, showing the best heat dissipation performance among different specimens (SI Figure S15). Based on the images recorded by the infrared thermal imager, the full-field thermal evolution process of the specimens further verifies the positive effect of  $\Phi_{LM}$  in improving the thermal conductivity for LM/PBSE composites (Figure 4d,e, SI Movie S2).

**3.5. Anti-Impact Property of LM/PBSE.** The above experimental results indicate that the LM/PBSE (PBSG: VMQ = 1:1,  $\Phi_{LM} = 15\%$ ) displays the optimal mechanical behavior and thermal property among all LM/PBSE composites. Therefore, the composite with the optimal proportion is utilized to analyze the environmental adaptability for LM/PBSE under complex loading conditions in the following discussions.

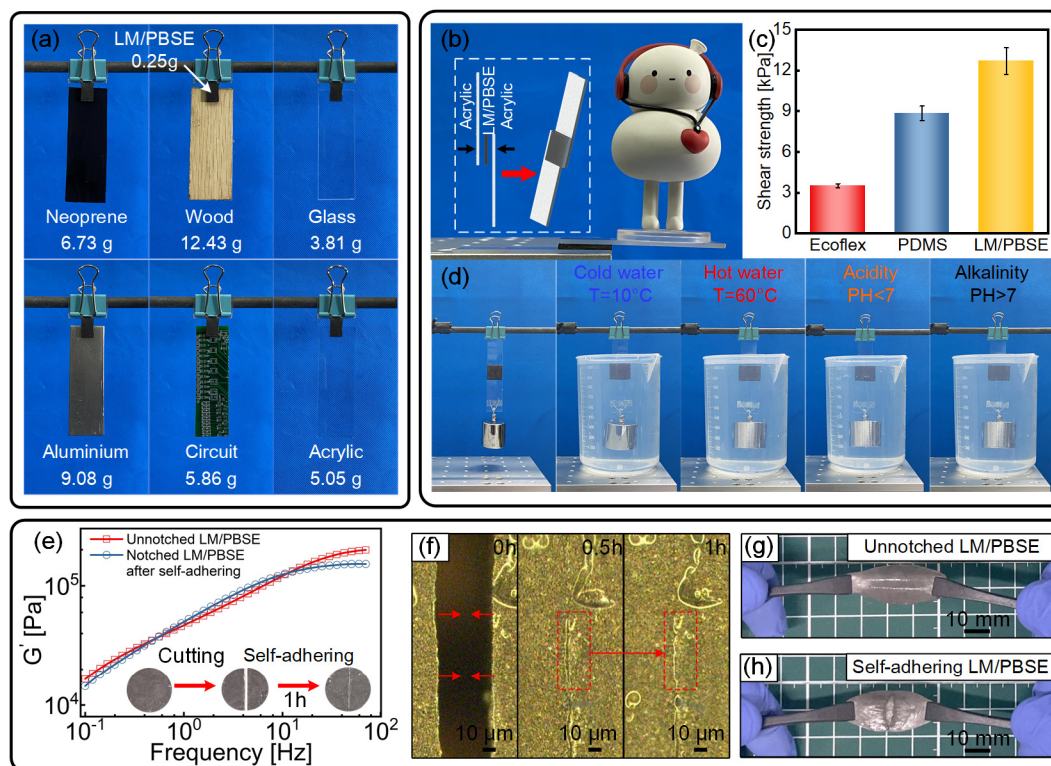


**Figure 6.** Adhesion Property of LM/PBSE. (a) Adhesion of LM/PBSE to the different material interfaces. (b) Out-of-plane loading capacity of LM/PBSE adhesive agent. (c) In-plane adhesion strength among the Ecoflex, PDMS, and LM/PBSE (Error bars: SD,  $n = 3$ ). (d) Adhesive adaptability of LM/PBSE in the air, cold water, hot water, acid solution, and alkaline solution. (e) Rheological curves between an unnotched LM/PBSE and a notched LM/PBSE after self-adhering. (f) Microscopic observation of the self-adhering process of the LM/PBSE. (g–h) Comparison of stretchability of an unnotched LM/PBSE and a notched LM/PBSE after self-adhering.

First, the drop-tower impact testing system is conducted to investigate the protective ability of the LM/PBSE (Figure 5a). The impact experiment without any specimen is designed as the control group, the maximum backing force values of the control group and experimental group are defined as  $F_0$  and  $F_{\max}$ , respectively. The attenuation ratio of the impact force ( $\eta$ ) was defined by the following formula (eq 3) (Figure 5b).

$$\eta = \frac{F_0 - F_{\max}}{F_0} \quad (3)$$

During the test, the anti-impact performance for another two common elastomers, polydimethylsiloxane (PDMS) and platinum catalyst Ecoflex-30 (Ecoflex) are also fabricated to compare with the softer PBSE matrix and LM/PBSE. It is shown in the force-time curves that the backing force of pure PBSE and LM/PBSE rapidly increases to the peak value and then decays symmetrically once the released drop tower contacts the specimen surface. The force-time curves of PDMS and Ecoflex specimens exhibit similar trends, except for the secondary rebound phenomenon at the end of the impact process. Obviously, the PDMS elastomer displays the worst anti-impact effect with the largest backing force at all of the releasing heights. Compared with the pure PBSE and LM/PBSE, the Ecoflex elastomer possesses a better impact attenuation ability at the releasing height of  $H = 10$  cm.

According to the rheological results of LM/PBSE, the elastomer shows a typical strain-rate stiffening effect at a higher loading frequency. The strain rates of impact loadings increase gradually with the improvement of releasing heights. Therefore, the strain rate stiffening effect of the PBSE system

becomes more prominent, leading to the surpassing of the anti-impact effect for pure PBSE and LM/PBSE against the Ecoflex elastomer at  $H = 20$  cm and  $H = 30$  cm. Besides, the coincidence of force-time curves of pure PBSE and LM/PBSE indicates that the embedding of LM droplets does not weaken the anti-impact performance of the PBSE matrix (Figure 5c–e). The calculation of attenuation rate  $\eta$  can further characterize the cushioning ability of the specimen. At a lower impact height of  $H = 10$  cm, the  $\eta$  of LM/PBSE elastomer has no obvious advantage over PDMS, even less than Ecoflex. As the release height increases, the  $\eta$  values for pure PBSE and LM/PBSE remain  $\eta = 0.6$ – $0.7$ , while those for Ecoflex elastomer decrease rapidly. Therefore, the LM/PBSE possesses a better anti-impact property (Figure 5f–h).

**3.6. Adhesion of LM/PBSE.** The polymer adhesive is also a complex material behavior influenced by chemistry, topology, and mechanics.<sup>45</sup> The characterization of the adhesive ability of LM/PBSE is helpful to understand its performance stability under complex loading conditions. It is demonstrated that the LM/PBSE elastomer exhibits a good adhesiveness to various material surfaces, such as rubber, wood, glass, metal, circuit, and acrylic (Figure 6a). To further verify the adhesion of LM/PBSE, an acrylic laminated structure is fabricated using a 20 mm  $\times$  20 mm  $\times$  2 mm LM/PBSE as the adhesive agent. The structure can withstand the bending moment generated by a 60 g doll (Figure 6b). In terms of the in-plane loading capacity, the LM/PBSE adhesive agent shows a higher adhesion strength (12.7 kPa) than the common silicone rubber Ecoflex (3.5 kPa) and PDMS (8.8 kPa) through the lap-shear experiment (Figure 6c, SI Figure S16). The LM/PBSE can



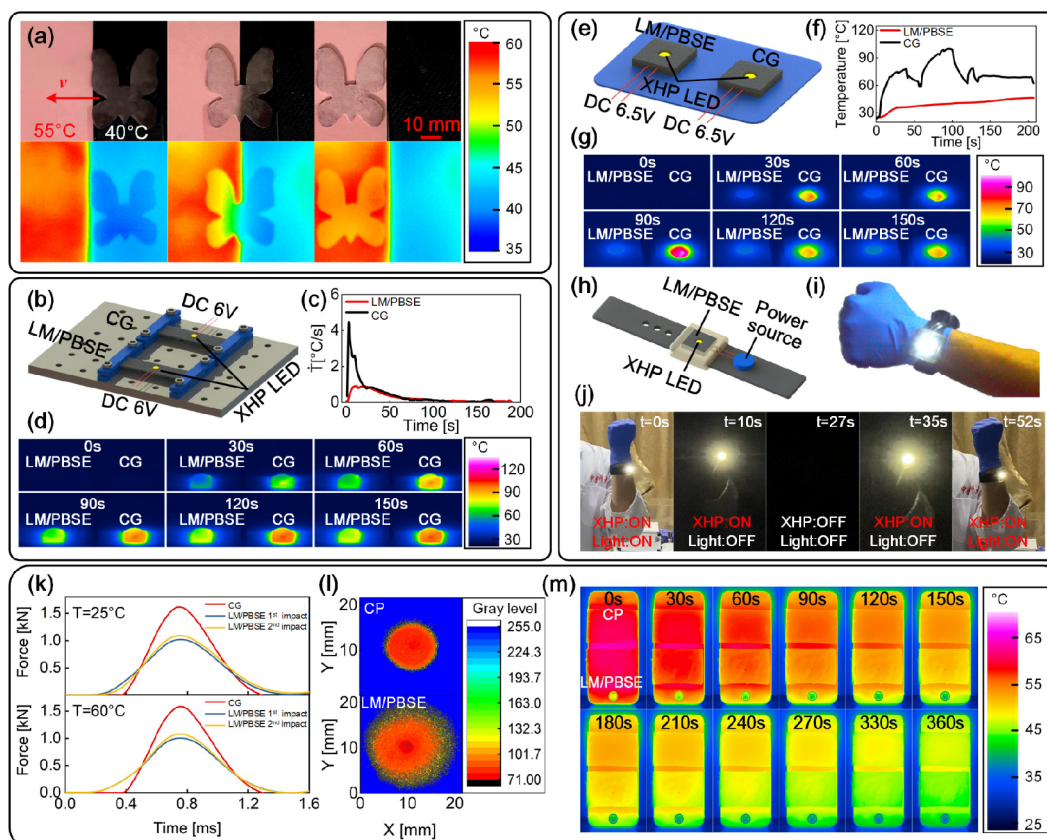


**Figure 7.** Applications of LM/PBSE. (a) The thermal camouflage ability of the LM/PBSE butterfly. (b–d) The thermal dissipation behavior for XHP LED at the rated voltage between the stretched LM/PBSE matrix and CG matrix. (e–g) The thermal dissipation behavior for XHP LED over the rated voltage between the LM/PBSE matrix and CG matrix. (h–j) The design of the LM/PBSE wearable wristband. (k–m) The comparison of the anti-impact property and heat dissipation property between the LM/PBSE elastomer and a commercial product.

easily lift a 200 g weight in the vertical direction, and similar loading capacities also can be observed in cold water, hot water, acidic solution (acetic acid), and alkaline solution (ammonium hydroxide). In summary, the LM/PBSE combines water repellency, temperature insensitivity as well as corrosion stability, and its adhesive behavior has excellent adaptability to the complex environment (Figure 6d). According to the previous research, the broken B–O dynamic bond can be recombined once the B atom and the O atom are close to each other.<sup>30</sup> Therefore, the LM/PBSE also exhibits an interesting self-adhering property. For instance, a cylindrical LM/PBSE specimen with a dimension of  $\Phi 20$  mm  $\times$  1 mm is cut along the diameter direction, and the fracture sections are recombined for 1 h without any modification. It is illustrated that the rheological behavior of the recombined LM/PBSE is analogous to that of the unnotched specimen (Figure 6e). The progressive self-adhering process of the fracture section is observed under the microscope images (Figure 6f). Besides, the recombined LM/PBSE also can be significantly stretched, similar to an unnotched specimen, indicating a remarkable self-adhering ability (Figure 6g–h).

#### 4. APPLICATIONS

According to the above discussion, the addition of LM droplets effectively enhances the mechanical and thermal properties of the PBSE matrix. Besides, the LM/PBSE also shows remarkable anti-impact, adhesion abilities. Therefore, It is valuable to explore the practical applications of LM/PBSE

composite. Similarly, the LM/PBSE (PBSG: VMQ = 1:1  $\Phi_{LM}$  = 15%) with the best mechanical and thermal performance is selected as the raw material for applications.

**4.1. Thermal Camouflage.** First, a thermal camouflage LM/PBSE butterfly is fabricated by dispersing thermochromic powders (transition temperature  $T_{tran} = 45$  °C, purchased from Zhicheng Technology Development Co., LTD, China) on the surface of the LM/PBSE composite. The thermochromic powders are stably attached to the surface of the butterfly due to the adhesive ability of the LM/PBSE. The surface color of the butterfly can rapidly and reversibly respond to the change in temperature (SI Figure S17). Further, the LM/PBSE butterfly is driven to cross the interface of two adjacent regions from 40 °C in the black region to 55 °C in the pink region. During this process, a rapid thermochromic reaction is observed for the partial area of the LM/PBSE entering the region of 55 °C, while the other area region of 40 °C remains black. The butterfly is invisible in the environmental field as if it were transparent (Figure 7a, SI Movie S3). Therefore, the LM/PBSE composite can quickly perceive the change in the external temperature field and make a color camouflage response.

**4.2. Stretchable Heat-Dissipation Matrix.** Second, previous research also demonstrates that the thermal conductivity of LM reinforced composite can be further improved with the elongation of LM droplets in the tensile process.<sup>21</sup> Inspired by this mechanism, the LM/PBSE is designed as the stretchable heat-dissipation matrix for high-power devices. An extreme high-power LED lamp (XHP-50/A,

6 V, purchased from CreeLED, U.S.) can be firmly attached to the surface of LM/PBSE due to the adhesive interactions with the circuit material. Under the rated power for the LED lamp, the thermal management ability of the LM/PBSE and control group (CG, PBSE: VMQ = 1:1, with low content of LM at  $\Phi_{LM} = 1\%$ ) are compared at a tension strain of  $\varepsilon = 0.75$  (Figure 7b). For the CG specimen, the temperature on the LED surface rapidly increases because of the heat accumulation in the working state. However, the heating rate of LED is effectively reduced by the LM/PBSE elastomer (Figure 7c). The heating phenomenon of LED is significantly alleviated on the LM/PBSE surface under tensile loadings, indicating its application prospect in heat dissipation for stretchable devices (Figure 7d, SI Movie S4).

It is worth noting that the heat dissipation ability of the LM/PBSE matrix above the LED rated power is also investigated to simulate the possible overload phenomena in practical applications. The LED is sandwiched by an LM/PBSE and another LM/PBSE with a circular hole. The input voltage for LED is set to be 6.5 V to simulate the overloading condition (Figure 7e). When the LED lamps are lit, the temperature of the LED sandwiched by the CG specimen increases rapidly. With the accumulation of a large amount of heat, the electric paths are inevitably affected. The fluctuation in the temperature–time curve represents the unpredictable flicker of LED, which seriously diminishes the lighting ability of LED. However, the LED sandwiched by the LM/PBSE displays a significantly lower surface temperature. The LM/PBSE can effectively dissipate the excess heat in overloading conditions, ensuring luminous stability for the LED (Figure 7f,g, SI Movie S5). Moreover, the LM/PBSE elastomer is assembled as a wearable wristband (Figure 7h). Combined with the heat dissipation ability and thermal stability, the wristband can supply steady and bright lighting for outdoor sports at night and on unpredictable power failure occasions. Moreover, the heat on the LED lamps can be effectively dissipated by LM/PBSE, avoiding the scalding of personnel (Figure 7i,j, SI Movies S6 and S7).

**4.3. Multifunctional Mobile Phone Shell.** Finally, based on the anti-impact property and high thermal conductivity, the LM/PBSE is shown to be an ideal candidate to fabricate the shell for mobile phones. The anti-impact behavior between the LM/PBSE and a commercial product mobile phone shell with the same thickness (CP, Xinku digital accessories Sales Co., LTD, China) is compared using the drop tower testing system. Especially, the releasing height of a blunt impactor is set to be 80 cm to simulate the falling conditions of mobile phones from the desktop or pocket. During the test, the maximum backing force of the LM/PBSE is only 1019 N at 25 °C and 1004 N at 60 °C, much smaller than the 1613 and 1582 N for the CP specimens, respectively. Besides, the mechanical behavior of the LM/PBSE rapidly recovers after the impact. The backing force increases only slightly against a secondary impact within a short time (Figure 7k). By placing the pressure-sensitive paper (LLW, Fujifilm, Japan) on the backside of the specimens, the stress distributions on backing materials also can be analyzed. Notably, the stress level is negatively correlated to the gray value. It is illustrated that the high-stress region is relatively concentrated in the center of the CP specimen. However, a wider stress distribution with less stress concentration in the central area is observed for the LM/PBSE. In this case, the shock wave is dissipated more evenly in the

LM/PBSE, and the composite displays a better buffering effect (Figure 7l).

To simulate the severe heating condition due to the excessive use of mobile phones, a mobile phone attached by the CP and LM/PBSE specimen is placed at room temperature after heating to 65 °C. It is shown that the LM/PBSE even shows a higher thermal conductivity compared to the CP specimen (Figure 7m, SI Figure S18 and Movie S8). Therefore, the LM/PBSE can quickly transform the excess thermal energy of mobile phones into the air and reduce the surface temperature of mobile phones.

## 5. CONCLUSION

In this work, a thermally conductive elastomer with both enhanced mechanical performance and thermal management effect is fabricated by dispersing LM microdroplets into the PBSE matrix. Proved by the microscopic observation, the liquid phase LM can generate large deformation with the movement of the PBSE matrix during the stretching process. Based on this unique mechanism, the fracture strain and toughness of the LM/PBSE elastomer are significantly enhanced. Meanwhile, the existence of LM plays a positive role in improving the heat-dissipation effect of LM/PBSE due to its high thermal conductivity. Besides, the LM/PBSE also displays good anti-impact and adhesion capacities, which greatly enhances its environmental adaptability under complex loading conditions. Therefore, as a high-performance elastomer with enhanced mechanical property and thermal conductivity, the LM/PBSE has great potential in thermally conductive applications.

## ■ ASSOCIATED CONTENT

### Supporting Information

The Supporting Information is available free of charge at <https://pubs.acs.org/doi/10.1021/acsami.2c04994>.

The correspondence between the volume fraction and mass fraction of LM (Table S1); The diameter distribution of LM droplets (Figure S1); The energy dispersive spectrometer (EDS) mapping of LM/PBSE (Figure S2); The comparison of the cold flow effect for PBSE and PBSE (Figure S3); The rheological testing of LM/PBSE specimens with different matrixes and LM volume fractions (Figure S4); The images of specimens of  $\Phi_{LM} = 0\%$  and  $\Phi_{LM} = 15\%$  LM/PBSE specimens with different matrixes before fracture strain (Figure S5); The microscopic structure of the LM droplets during the uniaxial tension process (Figure S6); The uniaxial cycling loading test for the LM/PBSE specimens with different matrixes under different strain amplitudes (Figure S7); The energy dissipation density and energy dissipation rate for the LM/PBSE specimens with different  $\Phi_{LM}$  for different matrixes (Figure S8); The diagram of the experimental device for crack propagation test and the representative morphology of specimens in the initial state and fracture state (Figure S9); The definition of the fracture toughness ( $\Gamma$ ) of the LM/PBSE specimen (Figure S10); The comparison of fracture strain ( $\varepsilon_f$ ) and toughness ( $\Gamma$ ) of solid inclusions and room-temperature liquid inclusions LM (Figure S11); The in situ observation during the crack propagation process (Figure S12); The comparison of the CTOD for pure PBSE matrix and LM/PBSE

elastomer (Figure S13); The comparison of the crack morphology for pure PBSE matrix and LM/PBSE elastomer (Figure S14); The rate of temperature change of specimens for the matrix PSBG: VMQ = 1:1 with different LM volume fractions (Figure S15); The diagram of the lap-shear experiment (Figure S16); The reversible ability of the color conversion of the LM/PBSE butterfly (Figure S17); The heat dispersion ability of CP and LM/PBSE (Figure S18) (PDF)

The comparison of the crack morphology for pure PBSE matrix and LM/PBSE elastomer (Movie S1) (MP4)

The full-field temperature distributions of the LM/PBSE on the surface of specimens during the heating and cooling process (Movie S2) (MP4)

The thermal camouflage ability of the LM/PBSE butterfly (Movie S3) (MP4)

The thermal dissipation behavior for XHP LED at the rated voltage between the stretched LM/PBSE matrix and CG matrix (Movie S4) (MP4)

The thermal dissipation behavior for XHP LED over the rated voltage between the LM/PBSE matrix and CG matrix (Movie S5) (MP4)

The LM/PBSE wearable wristband application for outdoor sports at night (Movie S6) (MP4)

The LM/PBSE wearable wristband application for unpredictable power failure occasions (Movie S7) (MP4)

The heat dissipation property of the LM/PBSE elastomer and a commercial product (Movie S8) (MP4)

## AUTHOR INFORMATION

### Corresponding Authors

**Yu Wang** – CAS Key Laboratory of Mechanical Behavior and Design of Materials, Department of Modern Mechanics, University of Science and Technology of China (USTC), Hefei 230027, P. R. China; Email: [wuyu@ustc.edu.cn](mailto:wuyu@ustc.edu.cn)

**Huaxia Deng** – CAS Key Laboratory of Mechanical Behavior and Design of Materials, Department of Modern Mechanics, University of Science and Technology of China (USTC), Hefei 230027, P. R. China; Email: [hxdeng@ustc.edu.cn](mailto:hxdeng@ustc.edu.cn)

**Xinglong Gong** – CAS Key Laboratory of Mechanical Behavior and Design of Materials, Department of Modern Mechanics, University of Science and Technology of China (USTC), Hefei 230027, P. R. China; [orcid.org/0000-0001-6997-9526](https://orcid.org/0000-0001-6997-9526); Email: [gongxl@ustc.edu.cn](mailto:gongxl@ustc.edu.cn)

### Authors

**Chunyu Zhao** – CAS Key Laboratory of Mechanical Behavior and Design of Materials, Department of Modern Mechanics, University of Science and Technology of China (USTC), Hefei 230027, P. R. China

**Liang Gao** – CAS Key Laboratory of Mechanical Behavior and Design of Materials, Department of Modern Mechanics, University of Science and Technology of China (USTC), Hefei 230027, P. R. China

**Yunqi Xu** – CAS Key Laboratory of Mechanical Behavior and Design of Materials, Department of Modern Mechanics, University of Science and Technology of China (USTC), Hefei 230027, P. R. China

**Ziyang Fan** – CAS Key Laboratory of Mechanical Behavior and Design of Materials, Department of Modern Mechanics,

University of Science and Technology of China (USTC), Hefei 230027, P. R. China

**Xujing Liu** – CAS Key Laboratory of Mechanical Behavior and Design of Materials, Department of Modern Mechanics, University of Science and Technology of China (USTC), Hefei 230027, P. R. China

**Yong Ni** – CAS Key Laboratory of Mechanical Behavior and Design of Materials, Department of Modern Mechanics, University of Science and Technology of China (USTC), Hefei 230027, P. R. China; [orcid.org/0000-0002-8944-5764](https://orcid.org/0000-0002-8944-5764)

**Shouhu Xuan** – CAS Key Laboratory of Mechanical Behavior and Design of Materials, Department of Modern Mechanics, University of Science and Technology of China (USTC), Hefei 230027, P. R. China; [orcid.org/0000-0002-8232-9736](https://orcid.org/0000-0002-8232-9736)

Complete contact information is available at: <https://pubs.acs.org/10.1021/acsami.2c04994>

## Notes

The authors declare no competing financial interest.

## ACKNOWLEDGMENTS

Financial supports from the National Natural Science Foundation of China (Nos. 11972337, 12132016, and 11972032) are gratefully acknowledged. This work was also partially carried out at the USTC Center for Micro and Nanoscale Research and Fabrication.

## ABBREVIATIONS

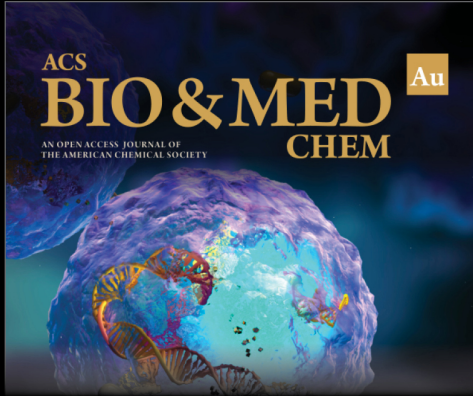
LM, liquid metal  
PBSG, polyborosiloxane gel  
VMQ, methyl vinyl silicone rubber  
PBSE, polyborosiloxane elastomer  
LM/PBSE, liquid metal/polyborosiloxane elastomer  
PDMS, polydimethylsiloxane  
CG, control group

## REFERENCES

- (1) Kou, Y.; Sun, K. Y.; Luo, J. P.; Zhou, F.; Huang, H. B.; Wu, Z. S.; Shi, Q. An Intrinsically Flexible Phase Change Film for Wearable Thermal Managements. *Energy Storage Mater.* **2021**, *34* (34), 508–514.
- (2) Sun, K. Y.; Dong, H. S.; Kou, Y.; Yang, H. N.; Liu, H. Q.; Li, Y. G.; Shi, Q. Flexible Graphene Aerogel-Based Phase Change Film for Solar-Thermal Energy Conversion and Storage in Personal Thermal Management Applications. *Chem. Eng. J.* **2021**, *419* (419), 129637.
- (3) Li, Y. H.; Li, W. J.; Sun, A. L.; Jing, M. F.; Liu, X. J.; Wei, L. H.; Wu, K.; Fu, Q. A Self-Reinforcing and Self-Healing Elastomer with High Strength, Unprecedented Toughness and Toom-Temperature Reparability. *Mater. Horiz.* **2021**, *8* (1), 267–275.
- (4) Lu, Q.; Jang, H. S.; Han, W. J.; Lee, J. H.; Choi, H. J. Stimuli-Responsive Graphene Oxide-Polymer Nanocomposites. *Macromol. Res.* **2019**, *27* (11), 1061–1070.
- (5) Tan, C. X.; Dong, Z. G.; Li, Y. H.; Zhao, H. G.; Huang, X. Y.; Zhou, Z. C.; Jiang, J. W.; Long, Y. Z.; Jiang, P. K.; Zhang, T. Y.; Sun, B. A High Performance Wearable Strain Sensor with Advanced Thermal Management for Motion Monitoring. *Nat. Commun.* **2020**, *11* (1), 3530.
- (6) Hu, R.; Liu, Y. D.; Shin, S. M.; Huang, S. Y.; Ren, X. C.; Shu, W. C.; Cheng, J. J.; Tao, G. M.; Xu, W. L.; Chen, R. K.; Luo, X. B. Emerging Materials and Strategies for Personal Thermal Management. *Adv. Energy Mater.* **2020**, *10* (17), 1903921.

- (7) Wang, Y. T.; Chen, L. Y.; Cheng, H.; Wang, B. J.; Feng, X. L.; Mao, Z. P.; Sui, X. F. Mechanically Flexible, Waterproof, Breathable Cellulose/Polypyrrole/Polyurethane Composite Aerogels as Wearable Heaters for Personal Thermal Management. *Chem. Eng. J.* **2020**, *402* (402), 126222.
- (8) Liu, S.; Wang, S.; Xuan, S. H.; Zhang, S. S.; Fan, X. W.; Jiang, H.; Song, P. A.; Gong, X. L. Highly Flexible Multilayered E-Skins for Thermal-Magnetic-Mechanical Triple Sensors and Intelligent Grippers. *ACS Appl. Mater. Interfaces* **2020**, *12* (13), 15675–15685.
- (9) Zhang, Y. F.; Huang, J. H.; Cao, M.; Liu, Z. Q.; Chen, Q. A Novel Flexible Phase Change Material with Well Thermal and Mechanical Properties For Lithium Batteries Application. *J. Energy Storage* **2021**, *44* (44), 103433.
- (10) Zhang, K.; Tao, P.; Zhang, Y. H.; Liao, X. P.; Nie, S. X. Highly Thermal Conductivity of CNF/AlN Hybrid Films for Thermal Management of Flexible Energy Storage Devices. *Carbohydr. Polym.* **2019**, *213* (213), 228–235.
- (11) Chen, Y. P.; Hou, X.; Kang, R. Y.; Liang, Y.; Guo, L. C.; Dai, W.; Nishimura, K.; Lin, C. T.; Jiang, N.; Yu, J. H. Highly Flexible Biodegradable Cellulose Nanofiber/Graphene Heat-Spreader Films with Improved Mechanical Properties and Enhanced Thermal Conductivity. *J. Mater. Chem. C* **2018**, *6* (46), 12739–12745.
- (12) Li, T. Q.; He, S. Y.; Stein, A.; Francis, L. F.; Bates, F. S. Synergistic Toughening of Epoxy Modified by Graphene and Block Copolymer Micelles. *Macromolecules* **2016**, *49* (24), 9507–9520.
- (13) Chen, S.; Wang, H. Z.; Zhao, R. Q.; Rao, W.; Liu, J. Liquid Metal Composites. *Matter* **2020**, *2* (6), 1446–1480.
- (14) Dickey, M. D. Stretchable and Soft Electronics Using Liquid Metals. *Adv. Mater.* **2017**, *29* (27), 1606425.
- (15) Yan, S.; Li, Y. X.; Zhao, Q. B.; Yuan, D.; Yun, G. L.; Zhang, J.; Wen, W. J.; Tang, S. Y.; Li, W. H. Liquid Metal-Based Amalgamation-Assisted Lithography for Fabrication of Complex Channels with Diverse Structures and Configurations. *Lab Chip* **2018**, *18* (5), 785–792.
- (16) Chang, H.; Zhang, P.; Guo, R.; Cui, Y. T.; Hou, Y.; Sun, Z. Q.; Rao, W. Recoverable Liquid Metal Paste with Reversible Rheological Characteristic for Electronics Printing. *ACS Appl. Mater. Interfaces* **2020**, *12* (12), 14125–14135.
- (17) Li, Y. Y.; Feng, S. X.; Cao, S. T.; Zhang, J. X.; Kong, D. S. Printable Liquid Metal Microparticle Ink for Ultrastretchable Electronics. *ACS Appl. Mater. Interfaces* **2020**, *12* (45), 50852–50859.
- (18) Hu, Y. J.; Zhuo, H.; Zhang, Y.; Lai, H. H.; Yi, J. W.; Chen, Z. H.; Peng, X. W.; Wang, X. H.; Liu, C. F.; Sun, R. C.; Zhong, L. X. Graphene Oxide Encapsulating Liquid Metal to Toughen Hydrogel. *Adv. Funct. Mater.* **2021**, *31* (51), 2106761.
- (19) Cademartiri, L.; Thuo, M. M.; Nijhuis, C. A.; Reus, W. F.; Tricard, S.; Barber, J. R.; Sodhi, R. N. S.; Brodersen, P.; Kim, C.; Chiechi, R. C.; Whitesides, G. M. Electrical Resistance of  $\text{Ag}^{\text{TS}}\text{-S}(\text{CH}_2)_{n-1}\text{CH}_3//\text{Ga}_2\text{O}_3/\text{EGaIn}$  Tunneling Junctions. *J. Phys. Chem. C* **2012**, *116* (20), 10848–10860.
- (20) Kazem, N.; Bartlett, M. D.; Majidi, C. Extreme Toughening of Soft Materials with Liquid Metal. *Adv. Mater.* **2018**, *30* (22), 1706594.
- (21) Bartlett, M. D.; Kazem, N.; Powell-Palm, M. J.; Huang, X. N.; Sun, W. H.; Malen, J. A.; Majidi, C. High Thermal Conductivity in Soft Elastomers with Elongated Liquid Metal Inclusions. *Proc. Natl. Acad. Sci. U.S.A.* **2017**, *114* (9), 2143–2148.
- (22) Moon, S.; Kim, H.; Lee, K.; Park, J.; Kim, Y.; Choi, S. Q. 3D Printable Concentrated Liquid Metal Composite with High Thermal Conductivity. *iScience* **2021**, *24* (10), 103183.
- (23) Zhou, L. Y.; Ye, J. H.; Fu, J. Z.; Gao, Q.; He, Y. 4D Printing of High-Performance Thermal-Responsive Liquid Metal Elastomers Driven by Embedded Microliquid Chambers. *ACS Appl. Mater. Interfaces* **2020**, *12* (10), 12068–12074.
- (24) Marco-Dufort, B.; Iten, R.; Tibbitt, M. W. Linking Molecular Behavior to Macroscopic Properties in Ideal Dynamic Covalent Networks. *J. Am. Chem. Soc.* **2020**, *142* (36), 15371–15385.
- (25) Boland, C. S.; Khan, U.; Ryan, G.; Barwich, S.; Charifou, R.; Harvey, A.; Backes, C.; Li, Z.; Ferreira, M. S.; Mobius, M. E.; Young, R. J.; Coleman, J. N. Sensitive Electromechanical Sensors Using Viscoelastic Graphene-Polymer Nanocomposites. *Science* **2016**, *354* (6317), 1257–1260.
- (26) Zhao, C. Y.; Gong, X. L.; Wang, S.; Jiang, W. Q.; Xuan, S. H. Shear Stiffening Gels for Intelligent Anti-Impact Applications. *Cell Rep. Phys. Sci.* **2020**, *1* (12), 100266.
- (27) Zhao, C. Y.; Wang, Y.; Ni, M. Y.; He, X. K.; Xuan, S. H.; Gong, X. L. Dynamic Behavior of Impact Hardening Elastomer: A Flexible Projectile Material with Unique Rate-Dependent Performance. *Compos. Part. A-Appl. S.* **2021**, *143* (143), 106285.
- (28) Wu, Q.; Xiong, H.; Peng, Y.; Yang, Y.; Kang, J.; Huang, G. S.; Ren, X. C.; Wu, J. R. Highly Stretchable and Self-Healing “Solid-Liquid” Elastomer with Strain-Rate Sensing Capability. *ACS Appl. Mater. Interfaces* **2019**, *11* (21), 19534–19540.
- (29) Zhang, S. S.; Wang, S.; Hu, T.; Xuan, S. H.; Jiang, H.; Gong, X. L. Study the Safeguarding Performance of Shear Thickening Gel by the Mechanoluminescence Method. *Compos. Part. B-Eng.* **2020**, *180* (180), 107564.
- (30) Wang, Y. P.; Ding, L.; Zhao, C. Y.; Wang, S.; Xuan, S. H.; Jiang, H.; Gong, X. L. A Novel Magnetorheological Shear-Stiffening Elastomer with Self-Healing Ability. *Compos. Sci. Technol.* **2018**, *168* (168), 303–311.
- (31) Zhang, J.; Liu, M.; Pearce, G.; Yu, Y. Y.; Sha, Z.; Zhou, Y. J.; Yuen, A. C. Y.; Tao, C. Y.; Boyer, C.; Huang, F.; Islam, M.; Wang, C. H. Strain Stiffening and Positive Piezoconductive Effect of Liquid Metal/Elastomer Soft Composites. *Compos. Sci. Technol.* **2021**, *201*, 108497.
- (32) Zhu, L. F.; Chen, Y. Z.; Shang, W. H.; Handschuh-Wang, S.; Zhou, X. H.; Gan, T. S.; Wu, Q. X.; Liu, Y. Z.; Zhou, X. C. Anisotropic Liquid Metal-Elastomer Composites. *J. Mater. Chem. C* **2019**, *7* (33), 10166–10172.
- (33) Wang, Z. J.; Xiang, C. P.; Yao, X.; Le Floch, P.; Mendez, J.; Suo, Z. G. Stretchable Materials of High Toughness and Low Hysteresis. *Proc. Natl. Acad. Sci. U.S.A.* **2019**, *116* (13), 5967–5972.
- (34) Yuan, F.; Wang, S.; Zhang, S. S.; Wang, Y.; Xuan, S. H.; Gong, X. L. A Flexible Viscoelastic Coupling Cable with Self-Adapted Electrical Properties and Anti-Impact Performance toward Shapeable Electronic Devices. *J. Mater. Chem. C* **2019**, *7* (27), 8412–8422.
- (35) Sang, M.; Wu, Y. X.; Liu, S.; Bai, L. F.; Wang, S.; Jiang, W. Q.; Gong, X. L.; Xuan, S. H. Flexible and Lightweight Melamine Sponge/MXene/Polyborosiloxane (MSMP) Hybrid Structure for High-Performance Electromagnetic Interference Shielding and Anti-Impact Safe-Guarding. *Compos. Part. B-Eng.* **2021**, *211*, 108669.
- (36) Park, J. E.; Kang, H. S.; Baek, J. H.; Park, T. H.; Oh, S. H.; Lee, H. S.; Koo, M.; Park, C. M. Rewritable, Printable Conducting Liquid Metal Hydrogel. *ACS Nano* **2019**, *13* (8), 9122–9130.
- (37) Hu, T.; Xuan, S. H.; Gao, Y. D.; Shu, Q.; Xu, Z. B.; Sun, S. S.; Li, J.; Gong, X. L. Smart Refreshable Braille Display Device Based on Magneto-Resistive Composite with Triple Shape Memory. *Adv. Mater. Technol.* **2022**, *7* (7), 2100777.
- (38) Li, Y. H.; Chen, J. Y.; Zhao, S.; Song, J. Z. Recent Advances on Thermal Management of Flexible Inorganic Electronics. *Micro-machines* **2020**, *11* (4), 390.
- (39) Song, P. A.; Wang, H. High-Performance Polymeric Materials through Hydrogen-Bond Cross-Linking. *Adv. Mater.* **2020**, *32* (18), 1901244.
- (40) Li, C. H.; Yang, H.; Suo, Z. G.; Tang, J. D. Fatigue-Resistant Elastomers. *J. Mech. Phys. Solids* **2020**, *134* (134), 103751.
- (41) Creton, C.; Ciccotti, M. Fracture and Adhesion of Soft Materials: A Review. *Rep. Prog. Phys.* **2016**, *79* (4), 046601.
- (42) Blaber, J.; Adair, B.; Antoniou, A. Ncorr: Open-Source 2D Digital Image Correlation Matlab Software. *Exp. Mech.* **2015**, *55* (6), 1105–1122.
- (43) Bartlett, M. D.; Fassler, A.; Kazem, N.; Markvicka, E. J.; Mandal, P.; Majidi, C. Stretchable, High-k Dielectric Elastomers through Liquid-Metal Inclusions. *Adv. Mater.* **2016**, *28* (19), 3726–3731.
- (44) Mayama, T.; Nishi, T.; Ohta, H.; Kanda, M. Thermal Diffusivity Measurement of Plastics by the Laser Flash Method. *J. Jpn. I. Met. Mater.* **2018**, *82* (11), 437–441.


(45) Yang, J. W.; Bai, R. B.; Chen, B. H.; Suo, Z. G. Hydrogel Adhesion: A Supramolecular Synergy of Chemistry, Topology, and Mechanics. *Adv. Funct. Mater.* **2020**, *30* (2), 1901693.




ACS  
**BIO & MED** Au  
AN OPEN ACCESS JOURNAL OF  
THE AMERICAN CHEMICAL SOCIETY  
**CHEM**

Editor-in-Chief: **Prof. Shelley D. Minteer**, University of Utah, USA

Deputy Editor  
**Prof. Squire J. Booker**  
Pennsylvania State University, USA

**Open for Submissions** 

pubs.acs.org/biomedchemau  ACS Publications  
Most Trusted. Most Cited. Most Read.